Ghost of Melts Past Beneath an Active Plate Boundary

Rachel Eleanor Bernard[1], Emily Joyce Chin[1], and Colin Murphy[2]

[1]Scripps Institution of Oceanography
[2]Amherst College

November 21, 2022

Abstract

We examine mid-lower crustal xenoliths erupted in Late Pleistocene to Holocene alkali basalt at San Quintin, Baja California, Mexico to investigate the role of partial melt in deep lithospheric deformation. Using major and trace element mineral chemistry data obtained from LA-ICP-MS and microstructural data obtained from EBSD, we cluster the crustal xenoliths into two groups based on textural and geochemical characteristics: Group (1) largely unfoliated two-pyroxene gabbros with minor amounts of olivine, and Group (2) gabbros with strong compositional foliation and up to 30% modal olivine. We interpret Group 1 xenoliths as representing underplated cumulates from basaltic magmas, whereas petrographic and quantitative microstructural data suggest Group 2 xenoliths record melt infiltration of pre-existing gabbros coeval with deformation, perhaps in a deep crustal shear zone. We propose this shear zone represents a deep lithospheric expression of the active transform plate boundary along the Baja California margin.

Ghost of Melts Past Beneath an Active Plate Boundary

R. E. Bernard[1,2], E. J. Chin[1], and C. Murphy[2]

[1] Scripps Institution of Oceanography, University of California, San Diego, La Jolla, CA, USA

[2] Amherst College, Amherst, MA, USA

Corresponding author: Rachel Bernard (rbernard@amherst.edu)

Key Points:

- Mid- lower crustal xenoliths from San Quintin in Baja California, Mexico characterized in terms of geochemistry and microstructure.

- Gabbroic xenoliths formed by underplated magma and record deformation in the presence of melt.

- Melt infiltration of pre-existing gabbros accommodated deformation in a deep crustal shear zone.

15 **Abstract**

16 We examine mid-lower crustal xenoliths erupted in Late Pleistocene to Holocene alkali basalt at

17 San Quintin, Baja California, Mexico to investigate the role of partial melt in deep lithospheric

18 deformation. Using major and trace element mineral chemistry data obtained from LA-ICP-MS

19 and microstructural data obtained from EBSD, we cluster the crustal xenoliths into two groups

20 based on textural and geochemical characteristics: Group (1) largely unfoliated two-pyroxene

21 gabbros with minor amounts of olivine, and Group (2) gabbros with strong compositional

22 foliation and up to 30% modal olivine. We interpret Group 1 xenoliths as representing

23 underplated cumulates from basaltic magmas, whereas petrographic and quantitative

24 microstructural data suggest Group 2 xenoliths record melt infiltration of pre-existing gabbros

25 coeval with deformation, perhaps in a deep crustal shear zone. We propose this shear zone

26 represents a deep lithospheric expression of the active transform plate boundary along the Baja

27 California margin.

28

29 **Plain Language Summary**

30 Xenoliths, rock fragments brought up rapidly to the surface by volcanism, provide a unique,

31 direct window into the nature of the deep lithosphere. Here we use xenoliths from the San

32 Quintin Volcanic Field to explore the role melt (magma) plays in deformation. Geochemistry and

33 analysis of the mineral textures within these rocks reveal two groups of xenoliths sourced from

34 the lower crust: one formed from accumulation of magma in the lower crust, and another formed

35 from the infiltration of melt into preexisting crustal rocks that were deformed during or prior to

36 this melt infiltration.

37

38 **1 Introduction**

39 Plate tectonics is governed by the underlying idea that lithospheric plates are rigid and

40 localize strain in narrow, well-defined zones. While this approximation is borne out amongst

41 most lithospheric plates on Earth, some plate boundaries defy this behavior, defined instead by

42 wide zones of seismicity and deformation (Gordon, 1998). A classic example of one such "soft"

43   margin is the Western US and Baja California, which is characterized by widespread low-

44   velocity mantle, magmatism, and anomalous seismicity (Suppe et al., 1973).

45   Strike slip faulting plays a significant role in accommodating motion between plates

46   (Woodcock, 1986), and characterizes much of the present-day North America-Pacific Plate

47   margin. Seismic data indicates that large continental strike slip faults, such as the San Andreas

48   Fault system extending along the entire California margin, may continue well into the lower

49   crust (Henstock et al., 1997) and even the upper mantle (Ford et al., 2014). A major unresolved

50   question is how deformation is distributed with depth and localized in the lithosphere. As

51   temperature and pressure increase with depth in the crust and upper mantle, deformation shifts

52   from brittle, narrow faults to ductile, wide shear zones (Fossen and Cavalcante, 2017; Wilson et

53   al., 2004). Moreover, increasing temperature with depth brings rocks closer to their melting

54   point, and so the role of partial melt becomes increasingly important in deep shear zones

55   (Davidson et al., 1994; Holtzman and Kendall, 2010). Even a small fraction of melt may be

56   important for lubricating the base of plate boundaries on a global scale (Schmerr, 2012;

57   Tharimena et al., 2017). Despite recognition of the role of melt in deep lithospheric deformation,

58   few direct observations exist because of the transitory nature of partial melt in the rock record.

59

2 Geologic Background

61   Xenoliths – fragments of deep lithospheric rocks brought up rapidly to the surface by volcanism

62   – provide a unique window into deep lithospheric deformation. Here we examine mid-lower

63   crustal xenoliths erupted in Late Pleistocene to Holocene basaltic cinder cones of OIB affinity at

64   San Quintin, Baja California, Mexico (Luhr et al., 1995) **(Fig. 1)**. The xenoliths were sourced

65   from the three localities within the San Quintin volcanic field with previously documented

66   xenoliths: Basu, Woodford, and Media Luna (Luhr et al., 1995) **(Fig. 1)**. These volcanoes

67   erupted close to the Santillan Y Barrera Line, which has been proposed as a potential fault-line

68   structure (Gastil et al., 1975), and which may still be active: In 1975, a swarm of earthquakes

69   occurred ~35 km northwest of the San Quintin volcanic field, which led to speculation of a

70   possible NW trending transcurrent fault in the area (Rebollar et al., 1982). The volcanoes at San

71   Quintin are unique amongst the extensive post-subduction magmatism of Baja California in

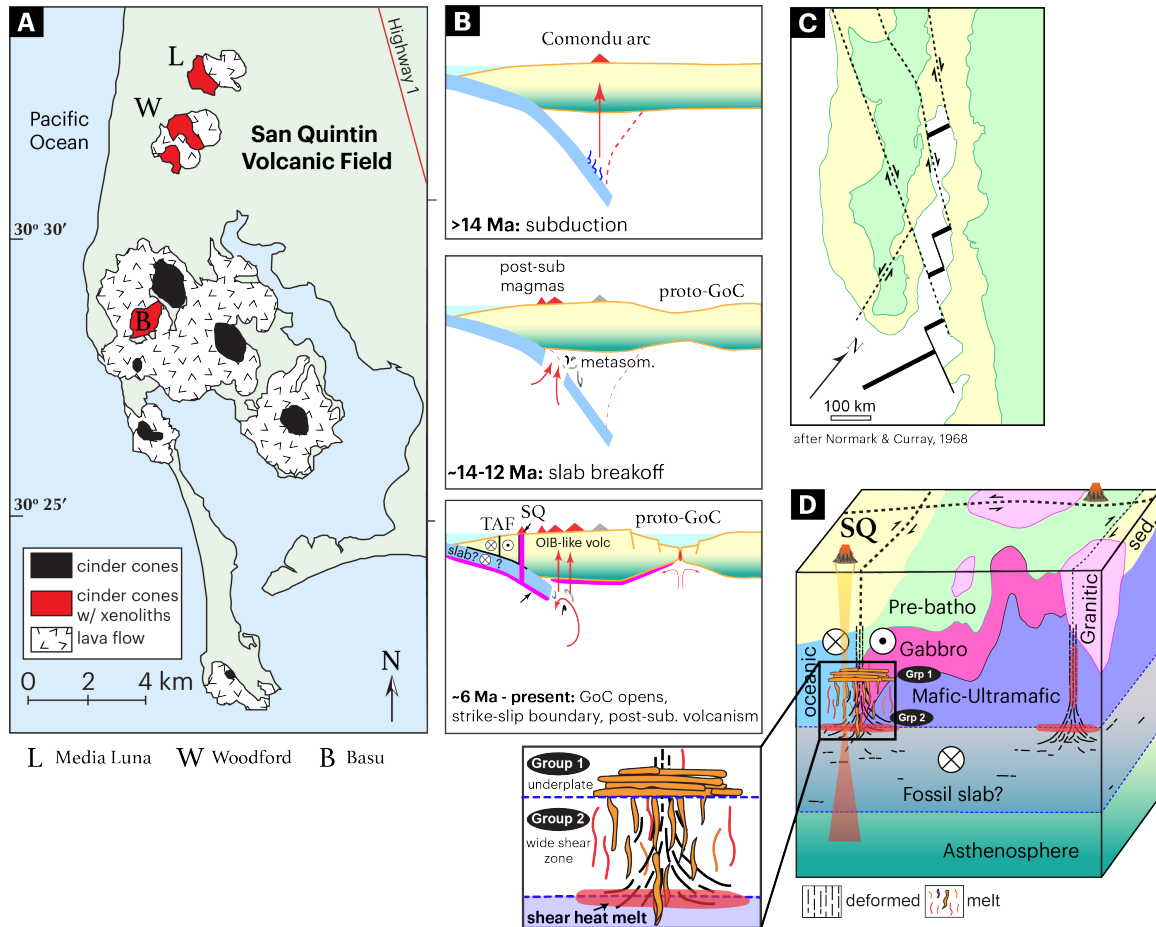72   being the only known source of lower crustal and upper mantle xenoliths along the peninsula.

Figure 1: Geologic setting and geodynamic overview of Baja California. A) Simplified map showing locations of volcanic features in the San Quintin Volcanic Field. The three Holocene cinder cones (M = Media Luna, W = Woodford, B = Basu) containing mantle and lower crustal xenoliths are shown in red. B) Schematic cross-sections showing development of the Baja California plate margin. >14 Ma, Baja was part of the Comondu arc along mainland Mexico. Between ~14 and 12 Ma, the margin transitioned out of subduction to rifting and initial opening of the Gulf of California. Slab window opens, post-subduction alkaline magmatism follows. From ~6 Ma to present, Gulf of California continues to open, strike-slip plate boundary develops, and post-subduction alkaline magmatism continues. Magenta layer represents hypothetical low-degree melt layer**.** C) Map view of one possible tectonic reconstruction of Baja California rifting from the mainland accommodated by a series of transcurrent faults coeval with the opening of the Gulf of California. D) Schematic block diagram showing tectonic and petrologic relationships as well as two possible melt sources. Group 1 xenoliths precipitate from crustally-derived melt, whereas Group 2 xenoliths are sourced slightly deeper and both Group 1 and 2 xenoliths are carried to the surface by a deeper-sourced melt that could be shear heating related.

73   San Quintin mantle xenoliths are well-studied examples of peridotite that experienced

74   significant plastic deformation and are renowned for their strongly porphyroclastic, highly

75   strained textures (Basu, 1977b). These deformed peridotites show strong olivine

76   crystallographic preferred orientation (CPO) and evidence of melt-rock reaction, which Cabanes

77   and Mercier (1988) and Palasse et al. (2012) interpreted as evidence for intense deformation in a

78   shallow shear zone in the upper mantle. Similarly strong olivine CPOs consistent with formation

79   at high temperatures and high average shear wave anisotropy have been reported in xenoliths

80   from beneath the San Andreas Fault system, suggesting that the fault shear zone extends to at

81   least 40 km depth (Titus et al., 2007). While San Quintin mantle xenoliths have been the subject

82   of several studies (Bacon and Carmichael, 1973; Basu, 1977a, b, 1979; Cabanes and Mercier,

83   1988; Palasse et al., 2012), only one published work on the fabrics of deep crustal xenoliths

84   exists to date (van der Werf et al., 2017). This study by van der Werf et al. (2017) examined the

85   rheological properties of San Quintin granulites and lherzolites, finding microstructures

86   consistent with deformation occurring at very low differential stresses in both the uppermost

87   lower crust and upper mantle via a combination of dislocation and grain-size-sensitive creep.

88   We present new mineral chemistry data on 11 lower crustal xenoliths, 10 of those for

89   which we also present microstructural analysis (detailed microstructural analyses of three

90   samples are the primary focus). Despite displaying a wide range of igneous and deformational

91   textures, lower crustal xenoliths consistently contain plagioclase, clinopyroxene, orthopyroxene,

92   spinel (oxides), and olivine. Our studied samples fall into two groups (Group 1 and 2) based on

93   textural and geochemical characteristics, which we discuss in the next sections.

94

95   **3 Methods**

96   Automated electron backscatter diffraction (EBSD) maps were acquired on an Oxford

97   Instruments Symmetry EBSD detector on a FEI Apreo LoVac field emission gun scanning

98   electron microscope (SEM) at the University of California San Diego (UCSD) using a step size

99   of $3 - 15$ μm, at a working distance between 26 to 28 mm, and voltage of 20 kV. Post-

100   processing, including noise reduction with a smoothing spline filter, was done using the open

101   source MTEX software (version 5.1.1) (Bachmann et al., 2011). MTEX was also used to

102   generate and analyze the data as EBSD maps and pole figures. Contoured pole figures were

103   generated using the density of the orientation distribution function (ODF) with a half-width of

104   10° plotted on the lower hemisphere. Grain boundaries are defined with a minimum angle of 10°.

105   Internal distortions within grains are quantified using the built-in MTEX functions grain

106   orientation spread (GOS) and Mis2Mean, both measured in degrees. Mis2Mean is the

107   misorientation between each pixel in a grain and the mean orientation of that grain. GOS is the

108   average Mis2Mean value of each grain (as an example, a grain with a high degree of internal

109   misorientation would have a high GOS). The strength of the CPO was quantified using the

110   dimensionless J-index, which varies from 1 (random orientation) to infinity (Bunge, 1982;

111   Mainprice et al., 2015). MTEX was also used to investigate shape preferred orientation (SPO) by

112   identifying the long axes of each grain within the mapped area and plotting the frequency of their

113   orientation relative to the horizontal as rose diagrams.

114   Major and trace elements were collected from polished thin sections using a Thermo

115   Fisher Scientific iCAP Qc Inductively Coupled Plasma Mass Spectrometry (ICP-MS) with New

116   Wave Research UP213 Laser Ablation system at UCSD. A laser spot size of 100 μm and a 5 Hz

117   repetition rate with a fluence of 3-3.5 J/cm^2 was used. For each spot, measurements were taken

118   for 60 seconds. Data was calibrated for each session (before, during, and after analyses of

119   unknowns) using the standard reference glasses NIST612, NIST610, BHVO-2g, BCR-2g,

120   and BIR-1g, and then corrected using Ca as the normalizing element.

121   Following LA-ICP-MS work, minerals were analyzed for major elements and WDS maps

122   were collected using the Cameca SX-100 electron microprobe with a CeB6 filament and 5 WDS

123   detectors at University of California Santa Barbara (20kV voltage, 10 nA beam current, 2 μm

124   spot size) using in-house standards. Additional data from one sample (THSQ4) was collected

125   using the Cameca SXFive-TACTIS microprobe with 5 WDS detectors and in-house standards at

126   the University of Massachusetts at Amherst (15kV, 20 nA, 2 μm). WDS mapping data were

127   input into XMapTools software (version 3.4.1) to calculate volume modal percentages using

128   representative points for each phase (Lanari et al., 2019).

129

4 Results

4.1 Microstructures

132   Group 1 consists of generally unfoliated, occasionally poikilitic two-pyroxene gabbros (with

133   minor olivine) exhibiting weak or no foliation (see Fig. S1 and Table S1 in the Supplement for

134   photomicrographs and details on petrographic characteristics, mineral modes, and average

135   mineral grain sizes). Some Group 1 gabbros are equigranular but with a shape-preferred

136   orientation (SPO) characterized by elongated plagioclase and/or pyroxenes defining a weak

137   foliation. The plagioclase and clinopyroxene grains often appear cotectic in these samples. Group

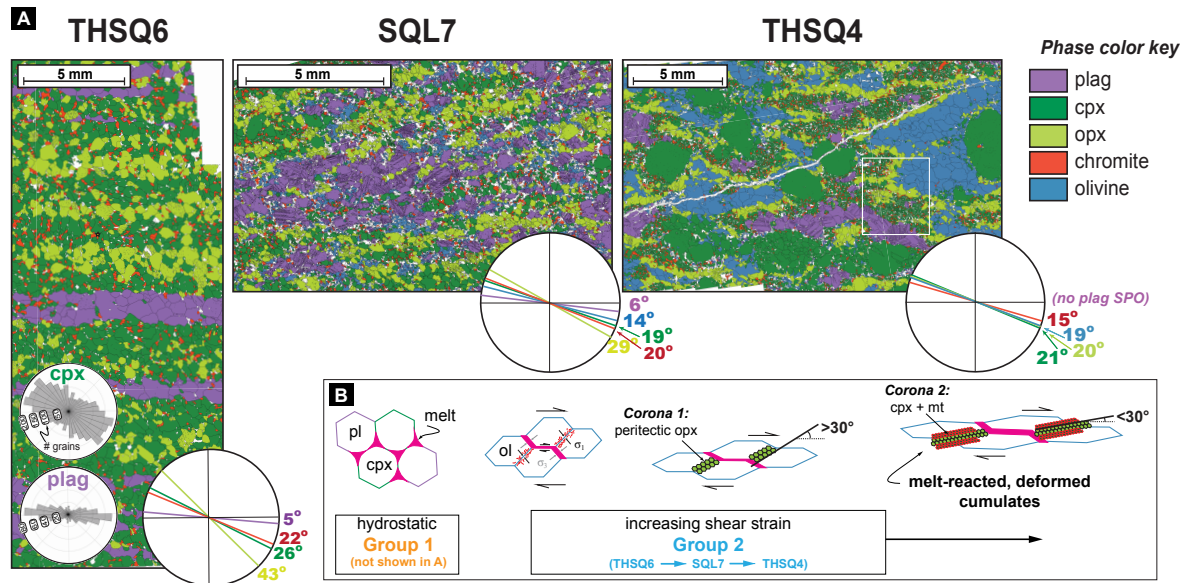138   2 consists of two-pyroxene gabbros with up to ~30% modal olivine (Fig. 2, Fig. S1, Table S1).

Figure 2: EBSD phase maps and diagrams of three Group 2 xenoliths. Rose diagrams, shown in two examples for sample THSQ6 (bottom left), were generated from EBSD data; the numbers on concentric circles represents a count of grains and the placement of the bars along those circles reflects the degrees between the orientation of a grain's long axis and the map's horizontal direction. Simplified versions (without concentric circles or bars) are shown in larger circles for each sample to illustrate the average offset (in degrees) between the grain long axes and foliation trace (horizontal). Rose diagrams for all phases in these samples are in the Supplement. The white rectangle in the THSQ4 phase map is the mapped area for **Fig. 3**. B) Conceptual model based on the experimental findings of Soustelle et al. (2014).

139   Texturally Group 2 differs from Group 1 samples in that the former are characterized by strong

140   compositional layering grading into disrupted layering with complex coronas mantling

141   clinopyroxene and olivine (Fig. 2). A multi-layered corona is shown in detail in Fig. 3, where

142   the first orthopyroxene corona mantles olivine, followed by a second corona around

143   orthopyroxene comprised of symplectite of fine-grained clinopyroxene and spinel.

144   Microstructures preserved in both Group 1 and 2 xenoliths record varying degrees of

145   deformation, due to both magmatic and solid state processes. Despite a weak SPO-defined

146   foliation, some Group 1 xenoliths have significant CPOs (Fig. S2). However, the generally low

147   internal grain misorientations and straight or curvilinear grain boundaries (Fig. S3, S4), supports

148   a magmatic – rather than crystal-plastic – origin to the weak foliation and/or CPO preserved in

149   Group 1 samples. This is also reinforced by the CPO types preserved in some Group 1 samples.

150   In THSQ2a, for example, plagioclase displays a CPO pattern consistent with axial-B or (010)-

151   fiber CPO, characterized by girdles within the foliation plane of [100] and (001), and (010) point

152   maxima oriented normal to foliation (Fig. S2). This CPO is common for plagioclase, thought to

153   be associated with magmatic, rather than solid state, deformation (Satsukawa et al., 2013). The
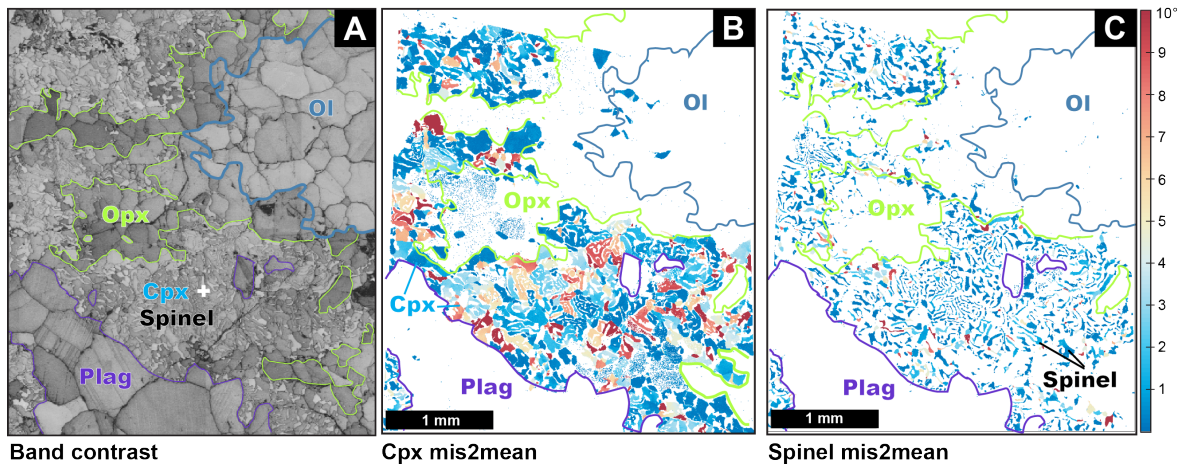
Figure 3: Higher resolution EBSD map (5 µm step size) of THSQ4 (rectangular area in Fig. 2a). A) Band contrast map; B-C) Mis2mean map of symplectite corona for clinopyroxene only (B) and spinel only (C).

154 straight or curvilinear grain boundaries and generally low internal misorientation also supports a

155 magmatic origin to any weak foliation or CPO preserved in Group 1 samples. SQW9, on the

156 other hand – a sample with lath-shaped olivine grains intergrown with plagioclase and

157 clinopyroxene surrounding clinopyroxene cores (Fig. S3) – is an outlier among Group 1 samples

158 with its strong intragranular misorientations in orthopyroxene and clinopyroxene grains and its

159 preservation of plagioclase type-P CPO, associated with plastic deformation (Satsukawa et al.,

160 2013). The orthopyroxene appears to have replaced clinopyroxene – an observation based on

161 textural relationships (orthopyroxene forming on the edges of clinopyroxene grains) and

162 identical orthopyroxene-clinopyroxene CPOs characterized by point maxima of [100] normal to

163 foliation, weak alignment of [010], and a girdled [001] within the foliation plane.

164 Group 2 samples show stronger compositional layering and significant SPO in

165 clinopyroxene, orthopyroxene, spinel, and olivine. Plagioclase rarely displays an SPO, and

166 instead appears as polygonal with straight grain boundaries and triple junctions. Some Group 2

167 samples, such as the strongly layered THSQ6, have no significant internal misorientation as

168 evident from the low GOS distribution across all grain sizes (Fig. 4, Fig. S4), and little to no

169 CPO in any phases (J indices < 2) (Fig. S2), but marked SPO in all minerals except plagioclase

170 (Fig. 2). Another feature of plagioclase in THSQ6 is abundant quadruple grain junctions, which

171 can be diagnostic of grain boundary sliding (Ashby and Verrall, 1973). Other Group 2 samples,

172 particularly those with greater olivine modes – such as SQL7 and THSQ4 – appear more

173 deformed, as they display strong SPO, moderate to strong internal misorientations in olivine and
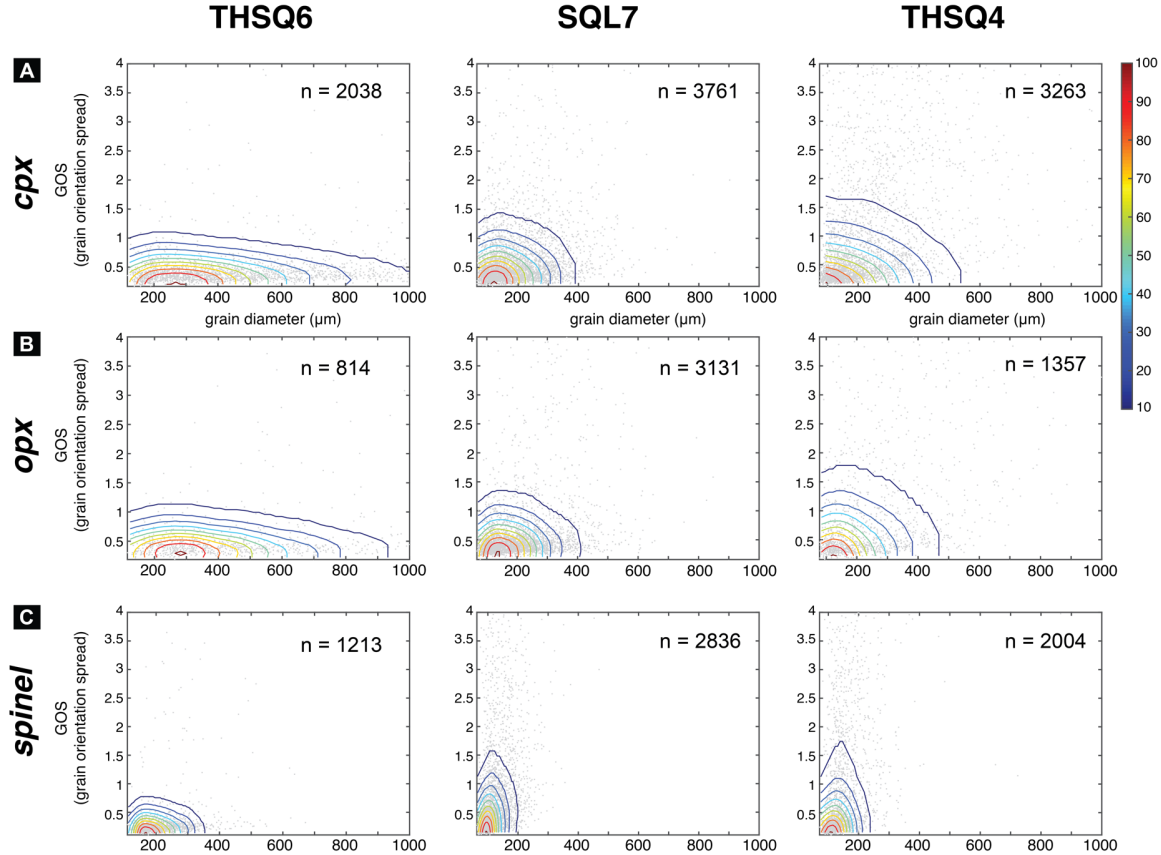
Figure 4: Grain orientation spread (GOS) vs. grain size for (A) clinopyroxene, (B) orthopyroxene, and (C) spinel in the three representative samples from Fig. 2. Individual data points shown in gray overlain by colored density contours. THSQ6 has a wider range of grain sizes and lower GOS in all phases, consistent with the interpretation that it is the least deformed of the three. THSQ4 has higher GOS values, consistent with the interpretation that it is the most deformed.

174   pyroxenes, moderate CPOs (J indices range from 1 to 4), and higher mineral GOS distribution

175   across all grain sizes (Fig. 4, Fig. S2, S4).

176   Interestingly, samples with coronas of clinopyroxene-spinel symplectites show

177   significant internal misorientations within the clinopyroxene (Fig. 3), suggesting deformation

178   occurred either after or during corona formation. THSQ4 is a particularly good example of this;

179   the symplectite clinopyroxene shows significantly greater internal deformation than the large,

180   relict clinopyroxenes outside of these symplectite layers (Fig. S5). This symplectite is the outer

181   layer of corona lenses, which themselves appear elongated in the lineation direction.

182   Deformation within the corona olivine has a strong CPO, SPO, and irregular grain boundaries

183   (Fig. S6).

4.2 Mineral Chemistry

184

185 We report incompatible trace element concentrations of orthopyroxenes (Table S2) and

186 clinopyroxenes (Fig. 5, Table S3), normalized to primitive mantle (McDonough and Sun, 1995),

187 for Group 1 and 2 crustal xenoliths and two San Quintin mantle xenoliths. Lower crustal xenolith

188 Group 1 is characterized by overall more enriched compositions (up to 10x primitive mantle)

189 compared to Group 2. Both groups have generally flat rare earth element (REE) patterns and

190 negative anomalies in Nb and Zr. Group 1 has a negative Sr anomaly (with respect to Ce and

191 Nd), whereas Group 2 xenoliths have positive Sr anomaly. This is more clearly shown in Fig. 5

192 where Group 1 clinopyroxenes have low Ti/Sm and low Sr/Nd, but Group 2 have elevated Ti/Sm

193 and Sr/Nd.

194 We analyzed major element compositions of clinopyroxene in the Group 2 xenoliths

195 THSQ6, SQ4 (texturally similar to SQL7), and THSQ4 and olivine in THSQ4 (Table S4).

196 Clinopyroxene in THSQ6 and SQ4 are homogeneous with respect to core-rim variation, with

197 average Mg# of 82 and 81, respectively. In contrast, THSQ4 clinopyroxene porphyroclast cores

198 have slightly lower Mg# (83) and CaO (19 wt.%) compared to rims (Mg# 85; CaO 23 wt.%).
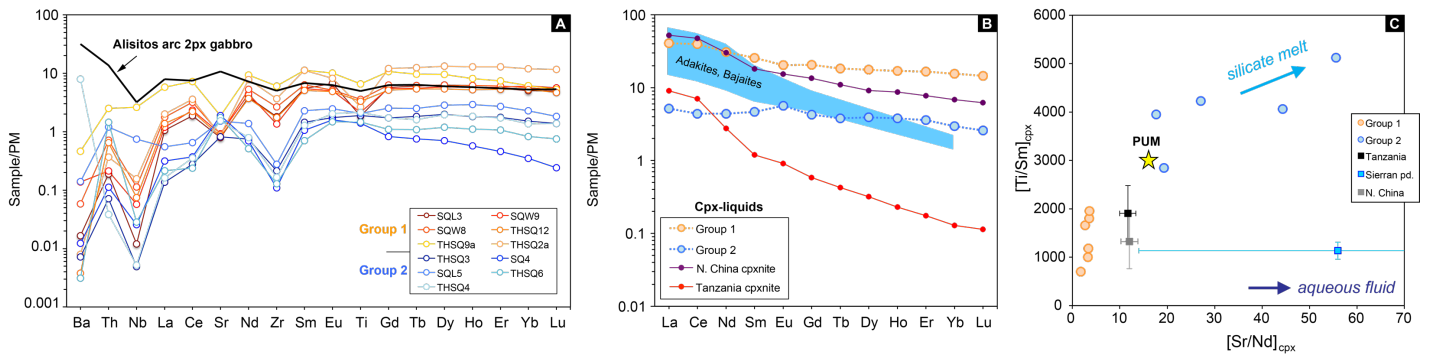
199 Olivine has an average Mg# of 76.

Figure 5: Clinopyroxene trace element geochemistry. A) Primitive mantle-normalized incompatible element diagram plotting Group 1 and Group 2 xenoliths. Two-pyroxene gabbro of the Alisitos arc is also shown (data from Morris et al. (2019)). B) Primitive mantle-normalized rare earth element (REE) diagram showing calculated liquids in equilibrium with clinopyroxenes using partition coefficients from Kelemen et al. (2003). Also shown for comparison are melts in equilibrium with clinopyroxene from lower crustal pyroxenites from North China Craton Chin et al. (2020) and cumulate clinopyroxenites from Tanzania Chin (2018). Field of adakite and bajaite from Castillo (2008). C) Ti/Sm versus Sr/Nd in clinopyroxenes from Group 1 and Group 2 xenoliths.

200

5 Discussion

5.1 Textural analysis: Evolution of SPO and corona textures

The compositional layering preserved in Group 2 rocks is often oblique to the elongation of minerals within these layers. We show this quantitatively using rose diagrams that plot long axis orientations of grains for each mineral. There is a clear, but variable, mineral SPO within Group 2 samples (Fig. 2, Fig. S7). Starting with the strongly layered sample THSQ6, orthopyroxene SPO is highly oblique (43°) to the foliation (horizontal aspect of the map). Note the apparent lack of olivine in THSQ6. With increasing modal olivine, the angle of orthopyroxene layering decreases, as observed in SQL7 (29°) to THSQ4 (20°) (Fig. 2). The SPO of clinopyroxene and spinel is also consistently oblique to foliation (~15-25°), though to a lesser extent than orthopyroxene on average. In contrast, plagioclase layers remain more or less parallel with foliation (within ~5°).

Interestingly, the amount of offset between orthopyroxene SPO and foliation appears to be a function of degree of strain, as shown quantitatively by GOS versus grain size plots (Fig. 4). In fact, with increasing disruption of the macro-scale layering across the three xenoliths in Fig. 2, all corona minerals (orthopyroxene, clinopyroxene, spinel) transition from a wide grain size distribution at consistently low GOS (i.e., all grains, regardless of size have little internal misorientation) to a narrow grain size distribution extending to higher GOS (i.e., smaller and more internally distorted grains) (Fig. 4).

The systematic variation in SPO angle with respect to foliation and concomitant increase of intragrain strain is strikingly similar to fabric evolution observed in experimentally deformed olivine + melt aggregates (Soustelle et al., 2014). Under hydrostatic conditions, the experiments show melt homogeneously distributed along olivine grain boundaries – e.g., similar to the texture of cumulate gabbros with interstitial crystallized melt, as represented by the Group 1 xenoliths. Soustelle et al. (2014) found that, with increasing shear strain, the melt + olivine aggregate experiences progressive melt-rock reaction and melt segregation into opening grain boundaries. Counteracting this is development of high dislocation density along grain boundaries compressed by the deformation; peritectic formation of orthopyroxene is favored along such boundaries.

229   With increasing shear strain, the orientation of peritectic orthopyroxene aligns with the shear

230   direction.

5.2 Nature of the melt

232   Silica-saturated (tholeiitic) basalts show the peritectic relationship Mg_2SiO_4 (olivine) + SiO_2

233   (melt) → $Mg_2Si_2O_6$ (orthopyroxene) at low pressure and dry conditions. The gabbroic

234   mineralogy of the San Quintin xenoliths indicates crystallization from basaltic melts. Yet,

235   constraints on the last equilibration P-T of the xenoliths indicates relatively deep conditions –

236   two-pyroxene geothermometry and phase equilibria modeling record last equilibration in the mid

237   to lower crust at 750 – 890 °C and 400 – 560 MPa (15-22 km) (van der Werf et al., 2017).

238   Further supporting a hot, high pressure origin, apparent partition coefficients (D_{REE}) between

239   orthopyroxene and clinopyroxene fall along the high-temperature equilibrium line (Lee et al.,

240   2007) (Fig. S8). These REE-based temperatures overlap those calculated for San Quintin mantle

241   xenoliths (Fig. S8), which have also been interpreted to be melt-refertilized (Palasse et al., 2012).

242   Given these near-solidus conditions for both the upper mantle and lower crust, and the similarity

243   to melt-present deformation experiments of Soustelle et al. (2014) discussed above, we interpret

244   the peritectic coronas in the San Quintin xenoliths as the product of mantle-derived, basaltic melt

245   crystallization coeval with deformation in the mid to lower crust.

246   However, at high pressure (1.5 GPa) and dry conditions, the peritectic reaction in

247   tholeiitic basaltic compositions disappears (Chen and Presnall, 1975). The addition of water to

248   the system at high pressure resurrects the peritectic reaction, and also expands the liquidus field

249   of clinopyroxene (Kushiro and Yoder, 1969). These phase equilibria could explain the corona

250   sequence of first orthopyroxene rimming olivine followed by clinopyroxene (+ spinel) (Fig. 3).

251   We propose that this corona sequence could develop during progressive crystallization of

252   interstitial, moderately hydrous melt as the cumulate cooled (de Haas et al., 2002; Joesten, 1986;

253   Otamendi et al., 2010). Unlike some of the coronas observed by Otamendi et al. in Famatina arc

254   cumulates, the San Quintin xenoliths lack an outer amphibole-rich corona, suggesting that the

255   melt was not as hydrous as those found in subduction zones.

256   Together with their typical cumulate fabrics, Group 1 xenoliths may represent

257   underplated cumulates from basaltic magmas, whereas the variably layered to disrupted,

258   coronitic textures of Group 2 record melt infiltration into pre-existing gabbros coeval with

259   deformation, perhaps in a deep crustal shear zone (Fig. 1d). Layered gabbros from Group 2,

260   such as THSQ6, could represent former Group 1 gabbros which were subsequently melt-reacted

261   and deformed; this transition is represented in SQL7 to THSQ4. Indeed, the Mg# of coexisting

262   olivine and clinopyroxene "paleoclasts" (i.e., large, relict grains not in coronas) show disturbed

263   equilibrium compared to olivine-clinopyroxene Mg# in layered gabbros (Lissenberg and Dick,

264   2008) (Table S4). This could be due to progressive reaction of paleoclasts with melt to form

265   complex coronas.

266

6 Geologic Interpretations

268   Petrographic and quantitative microstructural data support melt infiltration and deformation

269   occurring contemporaneously in San Quintin Group 2 lower crustal xenoliths. The timing of

270   these events, however, is not well constrained owing to lack of published radiometric age data on

271   the xenoliths. Based on geologic and tectonic context, two possibilities exist (cf.van der Werf et

272   al., 2017): 1) The xenoliths represent lower crust originally sourced from the North American

273   mainland (i.e. present-day Mexico) that rifted to the present day location of Baja California

274   during the Neogene – present opening of the Gulf of California, or 2) the xenoliths represent

275   more recent crust of either Pacific or North American heritage, deforming along the still active

276   transform plate boundary.

277   In the first scenario, the crust now represented by the San Quintin xenoliths could have

278   been originally associated with the long-lived Cretaceous subduction zone that characterized

279   much of the Western North American margin (Dickinson, 2004). The primitive mantle

280   normalized incompatible trace element pattern of two-pyroxene gabbro from the Alisitos arc,

281   formed during the Cretaceous in response to subduction beneath Mexico (Morris et al., 2019)

282   shows a mild arc signature, e.g., enrichment in large-ion lithophile elements (Ba, Th, Sr) relative

283   to fluid-immobile elements like Nb and Zr (Fig. 5). The rare earth elements are flat and similar

284   to MORB, supporting the hypothesis that the Alisitos terrane was a thin, juvenile oceanic arc

285   (Morris et al., 2019). Clinopyroxene trace element patterns of the San Quintin xenoliths,

286   particularly the Group 2 xenoliths, differ from Alisitos two-pyroxene gabbro in having an overall

287   more depleted (i.e., low Ba, Th, La) pattern (Fig. 5). We note, however, that side-by-side

288   comparisons between the Alisitos plutonic arc rocks and xenoliths may be questionable, as deep

289   crustal xenoliths often trend towards more primitive compositions compared to exhumed lower

290   crust (Rudnick and Fountain, 1995). Moreover, clinopyroxene trace elements have not been

291   reported for Alisitos gabbros.

292   In the second scenario, "de novo" melt infiltration and shearing occurred concomitant

293   with evolution of the transform plate boundary, with deformation along this boundary continuing

294   into the lower crust and uppermost mantle (Cabanes and Mercier, 1988; Palasse et al., 2012; van

295   der Werf et al., 2017) (Fig. 1d). Models of how the Baja terrane severed from the mainland and

296   sutured to the Pacific Plate (Lonsdale, 1995) point to movement along *en echelon* strike-slip

297   faults trending diagonal to the opening Gulf of California (Normark and Curray, 1968) (Fig. 1c).

298   Evidence of an early major transform fault is suggested by the northwest-trending, ~400 km long

299   Tosco-Abreojos (TAF) fault zone inferred to be active between 4.5 to ~12 My ago (Spencer and

300   Normark, 1979). Modeling of interplate coupling by Plattner et al. (2009) indicates that a

301   (minimum) shear stress of ~10 MPa along the TAF is reasonable for geological time scales; this

302   stress overlaps the range of 12-33 MPa found by van der Werf et al. (2017) using recrystallized

303   grain size paleopiezometry on San Quintin lower crustal xenoliths. Furthermore, fault activity

304   occurs near San Quintin along the Agua Blanca fault system (Allen et al., 1960), and seismic

305   activity ~30 km from San Quintin has occurred in the last few decades (Rebollar et al., 1982).

306   If the strike slip fault system accommodating Pacific-Baja plate movement does indeed

307   continue into the ductile regime, deformation would be more widely distributed at depth.

308   Geothermobarometry on San Quintin xenoliths by van der Werf et al. (2017) is consistent with a

309   hot geotherm beneath Baja, and so rocks would be nearer to their solidus, supporting a role for

310   melt-induced deformation in deep crustal shear zones. The question arises as to the geometry of

311   such a deep lithospheric shear zone. Although absent from northern Baja, shear velocity

312   anomalies at ~100 km depth have been interpreted as microplate remnants attached to the Baja

313   lithosphere (Wang et al., 2013); modeling based on this hypothesis (Negrete-Aranda et al., 2013)

314   proposed that shear heating along a low viscosity layer between the microplate and Baja

315   lithosphere induced partial melting consistent with patterns of post-subduction volcanism in the

316   region (e.g., Castillo, 2008). Rapid northwest movement of the Baja terrane could have dragged

317   the microplate and the intervening low-viscosity layer with it (Pikser et al., 2012). Ongoing

318   mantle upwelling in the Gulf of California would allow partial melt formed in the deep crust to

319   have multiple pathways along either horizontal decollements (i.e., associated with coupling of

320   relict microplate lithosphere to Baja lithosphere) or localized, mostly vertical shear zones,

321   perhaps reactived from inherited patterns of ancestral faulting associated with the opening of the

322   Gulf and breakaway of the Baja terrane (Fig. 1d).

323   The two hypotheses outlined above are not mutually exclusive. The San Quintin

324   xenoliths may have originated as pre-14 Ma arc lower crust, and either acquired their deformed

325   state during active subduction or more recently as the transform boundary evolved. Age data on

326   the San Quintin xenoliths would resolve the issue of an arc origin. Alternatively, the San Quintin

327   xenoliths represent post-14 Ma oceanic mid to lower crust along a lithospheric boundary

328   between the Pacific and Baja/North American plates, recently melt-infiltrated and deformed due

329   to continuation of strike-slip faults into the deep lithosphere. Calculated melts in equilibrium

330   with San Quintin clinopyroxenes suggest a MORB rather than subduction heritage (Fig. 5b).

331   Furthermore, clinopyroxene Ti/Sm and Sr/Nd ratios show a trend where Group 1 clinopyroxenes

332   have low Sr/Nd and low Ti/Sm whereas Group 2 clinopyroxenes have elevated Ti/Sm and high

333   Sr/Nd (Fig. 5c). Metasomatism dominated by aqueous fluids would elevate Sr/Nd but not

334   Ti/Sm, since Sr is highly fluid mobile but Ti is fluid immobile. As an example, clinopyroxene

335   from refertilized peridotites from the Sierra Nevada paleo-arc (Chin et al., 2012) extend to very

336   high Sr/Nd at low Ti/Sm, indicating interaction with subduction-derived melts and fluids. By

337   contrast, clinopyroxenes from the East African Rift (Chin, 2018) plot at low Sr/Nd, indicating

338   crystallization from or interaction with anhydrous melts. Group 2 San Quintin clinopyroxenes

339   have both high Sr/Nd and high Ti/Sm, distinct from Sierran arc xenoliths. We therefore propose

340   that melt rock interaction may have increased going from Group 1 to Group 2 xenoliths, but the

341   metasomatism was primarily silicate melt-dominated with a negligible fluid component.

342

343   **7 Conclusion**

344   We report new EBSD-based microstructural data and mineral chemistry on lower crustal

345   xenoliths from San Quintin, Baja California, Mexico. The xenoliths are categorized as Group 1

346   gabbronorites (<10% olivine, weak foliation and generally poikilitic textures, up to ~10x

347   primitive mantle trace element concentrations) and Group 2 gabbronorites (>10 % olivine, an

348   SPO that rotates with foliation, distinctive corona textures, and 1x or lower primitive mantle

349   trace element concentrations). We interpret Group 1 xenoliths as underplated cumulates of

350   mantle-derived, basaltic melts, whereas Group 2 xenoliths represent melt-infiltrated gabbros

351   from a deep crustal shear zone. Gradual rotation of SPO to align with foliation has been

352   previously found to occur during deformation experiments on sheared olivine + melt aggregates.

353   We also find that the extent of intragranular strain, exemplified in crystallized melt coronas,

354   increases as SPO and foliation orientation coincide, further supporting that deformation and melt

355   went hand-in-hand. Collectively, the textures and geochemistry of Group 2 xenoliths suggest

356   that active strike-slip tectonics extends into the deep lithosphere, and that melt may play a key

357   role in facilitating deformation.

358

359   Acknowledgments, Samples, and Data

365
366

References

Allen, C.R., Silver, L.T., Stehli, F.G., 1960. Agua Blanca fault—A major transverse structure of northern Baja California, Mexico. *Geological Society of America Bulletin* 71, 467-482.

Ashby, M., Verrall, R., 1973. Diffusion-accommodated flow and superplasticity. *Acta metallurgica* 21, 149-163.

Bachmann, F., Hielscher, R., Schaeben, H., 2011. Grain detection from 2d and 3d EBSD data: Specification of the MTEX algorithm. *Ultramicroscopy* 111, 1720-1733.

Bacon, C., Carmichael, I., 1973. Stages in the PT path of ascending basalt magma: an example from San Quintin, Baja California. *Contributions to Mineralogy and Petrology* 41, 1-22.

Basu, A.R., 1977a. Olivine-spinel equilibria in lherzolite xenoliths from San Quintin, Baja California. *Earth and Planetary Science Letters* 33, 443-450.

Basu, A.R., 1977b. Textures, microstructures and deformation of ultramafic xenoliths from San Quintin, Baja California. *Tectonophysics* 43, 213-246.

Basu, A.R., 1979. Geochemistry of ultramafic xenoliths from San Quintin, Baja California. *The mantle sample: inclusion in kimberlites and other volcanics* 16, 391-399.

Bunge, H., 1982. Texture Analysis in Materials Science. Butterworth's, London.

Cabanes, N., Mercier, J.-C., 1988. Insight into the upper mantle beneath an active extensional zone: the spinel-peridotite xenoliths from San Quintin (Baja California, Mexico). *Contributions to Mineralogy and Petrology* 100, 374-382.

Castillo, P.R., 2008. Origin of the adakite–high-Nb basalt association and its implications for postsubduction magmatism in Baja California, Mexico. *GSA Bulletin* 120, 451-462.

Chen, C., Presnall, D., 1975. The system Mg2SiO4-SiO2 at pressures up to 25 kilobars. *American Mineralogist* 60, 398-406.

Chin, E.J., 2018. Deep crustal cumulates reflect patterns of continental rift volcanism beneath Tanzania. *Contributions to Mineralogy and Petrology* 173, 85.

Chin, E.J., Lee, C.-T.A., Luffi, P., Tice, M., 2012. Deep Lithospheric Thickening and Refertilization beneath Continental Arcs: Case Study of the P, T and Compositional Evolution of Peridotite Xenoliths from the Sierra Nevada, California. *Journal of Petrology* 53, 477-511.

Chin, E.J., Soustelle, V., Liu, Y., 2020. An SPO-induced CPO in composite mantle xenoliths correlated with increasing melt-rock interaction. *Geochimica et Cosmochimica Acta* 278, 199-218.

Davidson, C., Schmid, S.M., Hollister, L.S., 1994. Role of melt during deformation in the deep crust. *Terra Nova* 6, 133-142.

de Haas, G.-J.L., Nijland, T.G., Valbracht, P.J., Maijer, C., Verschure, R., Andersen, T., 2002. Magmatic versus metamorphic origin of olivine-plagioclase coronas. *Contributions to Mineralogy and Petrology* 143, 537-550.

Dickinson, W.R., 2004. Evolution of the North American Cordillera. *Annu. Rev. Earth Planet. Sci.* 32, 13-45.

Ford, H.A., Fischer, K.M., Lekic, V., 2014. Localized shear in the deep lithosphere beneath the San Andreas fault system. *Geology* 42, 295-298.

Fossen, H., Cavalcante, G.C.G., 2017. Shear zones–A review. *Earth-Science Reviews* 171, 434-455.

Gastil, R.G., Phillips, R.P., Allison, E.C., 1975. Reconnaissance geology of the state of Baja California. Geological Society of America.

Gordon, R.G., 1998. The plate tectonic approximation: Plate nonrigidity, diffuse plate boundaries, and global plate reconstructions. *Annual Review of Earth and Planetary Sciences* 26, 615-642.

Henstock, T.J., Levander, A., Hole, J.A., 1997. Deformation in the lower crust of the San Andreas fault system in northern California. *Science* 278, 650-653.

Holtzman, B.K., Kendall, J.M., 2010. Organized melt, seismic anisotropy, and plate boundary lubrication. *Geochemistry, Geophysics, Geosystems* 11.

Joesten, R., 1986. The role of magmatic reaction, diffusion and annealing in the evolution of coronitic microstructure in troctolitic gabbro from Risör, Norway. *Mineralogical Magazine* 50, 441-467.

Kelemen, P.B., Yogodzinski, G.M., Scholl, D.W., 2003. Along-strike variation in the Aleutian island arc: Genesis of high Mg# andesite and implications for continental crust. *Inside the Subduction Factory*, Geophys. Monogr. Ser 138, 223-276.

Kushiro, I., Yoder, H.S., 1969. Melting of forsterite and enstatite at high pressures under hydrous conditions. *Carnegie Inst Washington Yearb* 67, 153-161.

Lanari, P., Vho, A., Bovay, T., Airaghi, L., Centrella, S., 2019. Quantitative compositional mapping of mineral phases by electron probe micro-analyser. Geological Society of London, Special Publications, **478**, 39-63.

Lee, C.-T.A., Harbert, A., Leeman, W.P., 2007. Extension of lattice strain theory to mineral/mineral rare-earth element partitioning: An approach for assessing disequilibrium and

developing internally consistent partition coefficients between olivine, orthopyroxene, clinopyroxene and basaltic melt. *Geochimica et Cosmochimica Acta* 71, 481-496.

Lissenberg, C.J., Dick, H.J., 2008. Melt–rock reaction in the lower oceanic crust and its implications for the genesis of mid-ocean ridge basalt. *Earth and Planetary Science Letters* 271, 311-325.

Lonsdale, P., 1995. Segmentation and disruption of the East Pacific Rise in the mouth of the Gulf of California. *Marine Geophysical Researches* 17, 323-359.

Luhr, J.F., Aranda‐Gómez, J.J., Housh, T.B., 1995. San Quintin volcanic field, Baja California Norte, Mexico: geology, petrology, and geochemistry. *Journal of Geophysical Research: Solid Earth* 100, 10353-10380.

Mainprice, D., Bachmann, F., Hielscher, R., Schaeben, H., 2015. Descriptive tools for the analysis of texture projects with large datasets using MTEX: strength, symmetry and components. Geological Society, London, Special Publications 409, 251-271.

McDonough, W.F., Sun, S.s., 1995. The composition of the Earth. *Chemical Geology* 120, 223-253.

Morris, R.A., DeBari, S.M., Busby, C., Medynski, S., Jicha, B.R., 2019. Building arc crust: plutonic to volcanic connections in an extensional oceanic arc, the southern Alisitos arc, Baja California. *Journal of Petrology* 60, 1195-1228.

Negrete-Aranda, R., Contreras, J., Spelz, R.M., 2013. Viscous dissipation, slab melting, and post-subduction volcanism in south-central Baja California, Mexico. *Geosphere* 9, 1714-1728.

Normark, W.R., Curray, J.R., 1968. Geology and structure of the tip of Baja California, Mexico. *Geological Society of America Bulletin* 79, 1589-1600.

Otamendi, J., Cristofolini, E., Tibaldi, A., Quevedo, F., Baliani, I., 2010. Petrology of mafic and ultramafic layered rocks from the Jaboncillo Valley, Sierra de Valle Fértil, Argentina: implications for the evolution of magmas in the lower crust of the Famatinian arc. *Journal of South American Earth Sciences* 29, 685-704.

Palasse, L., Vissers, R., Paulssen, H., Basu, A., Drury, M., 2012. Microstructural and seismic properties of the upper mantle underneath a rifted continental terrane (Baja California): An example of sub-crustal mechanical asthenosphere? *Earth and Planetary Science Letters* 345, 60-71.

Pikser, J.E., Forsyth, D.W., Hirth, G., 2012. Along-strike translation of a fossil slab. *Earth and Planetary Science Letters* 331, 315-321.

Plattner, C., Malservisi, R., Govers, R., 2009. On the plate boundary forces that drive and resist Baja California motion. *Geology* 37, 359-362.

505

506 Rebollar, C., Reyes, A., Reichle, M., 1982. Estudio del enjambre de San Quintin, Baja california,
507 México, ocurrido durante 1975. *Geofísica Internacional* 21.

508

509 Rudnick, R.L., Fountain, D.M., 1995. Nature and composition of the continental crust: A lower
510 crustal perspective. *Rev. Geophys.* 33, 267-309.

511

512 Satsukawa, T., Ildefonse, B., Mainprice, D., Morales, L., Michibayashi, K., Barou, F., 2013. A
513 database of plagioclase crystal preferred orientations (CPO) and microstructures–implications for
514 CPO origin, strength, symmetry and seismic anisotropy in gabbroic rocks. *Solid Earth* 4, 511-
515 542.

516

517 Schmerr, N., 2012. The Gutenberg discontinuity: Melt at the lithosphere-asthenosphere
518 boundary. *Science* 335, 1480-1483.

519

520 Soustelle, V., Walte, N.P., Manthilake, M.G.M., Frost, D.J., 2014. Melt migration and melt-rock
521 reactions in the deforming Earth‚Äôs upper mantle: Experiments at high pressure and
522 temperature. *Geology* 42, 83-86.

523

524 Spencer, J.E., Normark, W.R., 1979. Tosco-Abreojos fault zone: A Neogene transform plate
525 boundary within the Pacific margin of southern Baja California, Mexico. *Geology* 7, 554-557.

526

527 Suppe, J., Powell, C., Berry, R., 1973. Regional topography, seismicity, volcanism, and the
528 present-day tectonics of the western United States. Stanford Univ. Pubs. Geol. Sci. 13, 181.

529

530 Tharimena, S., Rychert, C., Harmon, N., 2017. A unified continental thickness from seismology
531 and diamonds suggests a melt-defined plate. *Science* 357, 580-583.

532

533 Titus, S.J., Medaris Jr, L.G., Wang, H.F., Tikoff, B., 2007. Continuation of the San Andreas fault
534 system into the upper mantle: evidence from spinel peridotite xenoliths in the Coyote Lake
535 basalt, central California. *Tectonophysics* 429, 1-20.

536

537 van der Werf, T., Chatzaras, V., Kriegsman, L.M., Kronenberg, A., Tikoff, B., Drury, M.R.,
538 2017. Constraints on the rheology of lower crust in a strike-slip plate boundary: Evidence from
539 the San Quintin xenoliths, Baja California, Mexico. *Solid Earth* 8, 1211-1239.

540

541 Wang, Y., Forsyth, D.W., Rau, C.J., Carriero, N., Schmandt, B., Gaherty, J.B., Savage, B., 2013.
542 Fossil slabs attached to unsubducted fragments of the Farallon plate. *Proceedings of the National*
543 *Academy of Sciences* 110, 5342-5346.

544

545 Wilson, C.K., Jones, C.H., Molnar, P., Sheehan, A.F., Boyd, O.S., 2004. Distributed deformation
546 in the lower crust and upper mantle beneath a continental strike-slip fault zone: Marlborough
547 fault system, South Island, New Zealand. *Geology* 32, 837-840.

548

549 Woodcock, N.H., 1986. The role of strike-slip fault systems at plate boundaries. Philosophical
550 Transactions of the Royal Society of London. Series A, Mathematical and Physical Sciences 317,
551 13-29.

552